

the filaments and grains. They might be related to the "dark puffs" seen in the blue wing of  $H\alpha$  (11) and to running penumbral waves, or both.

These space-based high-resolution movies of a sunspot have been successful in elucidating sunspot phenomena, and they highlight the severe handicap imposed by terrestrial atmospheric turbulence on visible-light solar observations. These data are only a hint of what can be done with a stabilized solar telescope in space. Further space-based observations coupled with image processing systems capable of handling large amounts of data will revolutionize solar physics and our understanding of stellar atmospheres.

#### REFERENCES AND NOTES

1. A. M. Title *et al.*, *Adv. Space Res.* **6**, 253 (1986).
2. Movies made from the raw data show strong brightness fluctuations with spatial and temporal scales characteristic of  $p$ -mode oscillations (that is, larger than 5000 km and about 5 minutes); these fluctuations make it difficult to follow the evolution of smaller structures. A review on solar oscillations is given by J. Christensen-Dalsgaard, D. Gough, and J. Toomre [*Science* **229**, 923 (1985)]. The SOUP data did not have sufficient resolution in Fourier space to

- resolve individual  $p$ -mode ridges; we were able to distinguish the fundamental mode, however.
3. T. D. Kinman, *Mon. Not. R. Astron. Soc.* **112**, 425 (1952).
  4. N. R. Sheeley and A. Bhatnagar, *Sol. Phys.* **19**, 338 (1971).
  5. J. M. Beckers, *ibid.* **3**, 258 (1968).
  6. H. I. Abdusamatov and V. A. Krat, *ibid.* **14**, 132 (1970).
  7. E. Wiehr, G. Stellmacher, M. Knölker, H. Grosser, *Astron. Astrophys.* **155**, 402 (1986).
  8. R. L. Moore, in *Proceedings of the Physics of Sunspots*, Sunspot, NM, 14 to 17 July 1981, L. E. Cram and J. H. Thomas, Eds. (available from Sacramento Peak Observatory, Sunspot, NM), pp. 259-311.
  9. L. J. November, G. W. Simon, T. D. Tarbell, A. M. Title, S. H. Ferguson, in *Proceedings of the Second Workshop on Problems in High Resolution Solar Observations*, Boulder, CO, 15 to 17 September 1986, R. G. Athay, Ed. (National Center for Atmospheric Research, Boulder, CO, in press).
  10. R. Muller, *Sol. Phys.* **48**, 101 (1976).
  11. R. L. Moore and F. Tang, *ibid.* **41**, 81 (1975).
  12. We thank the additional members of the SOUP team for their contributions: L. Acton, D. Duncan, S. Ferguson, M. Finch, Z. Frank, G. Kelly, R. Lindgren, M. Morrill, T. Pope, R. Reeves, and R. Rehse (Lockheed Palo Alto Research Laboratory); G. Simon (Air Force Geophysics Laboratory, Sunspot, NM); J. Harvey, J. Leibacher, and W. Livingston (National Solar Observatory, Tucson, AZ); and L. November and J. Zirker (National Solar Observatory, Sunspot, NM). Supported by NASA contracts NAS8-32805 and NAS5-26813 and by the Lockheed Independent Research Fund.
- 26 May 1987; accepted 17 September 1987

## Ultraviolet Observations of Solar Fine Structure

KENNETH P. DERE, JOHN-DAVID F. BARTOE,  
GUENTER E. BRUECKNER, JOHN W. COOK, DENNIS G. SOCKER

The High Resolution Telescope and Spectrograph was flown on the Spacelab-2 shuttle mission to perform extended observations of the solar chromosphere and transition zone at high spatial and temporal resolution. Ultraviolet spectroheliograms show the temporal development of macrospicules at the solar limb. The C IV transition zone emission is produced in discrete emission elements that must be composed of exceedingly fine (less than 70 kilometers) subresolution structures.

THE NAVAL RESEARCH LABORATORY High Resolution Telescope and Spectrograph (HRTS) was one of four instruments to perform solar observations during the Spacelab-2 shuttle mission, which flew from 29 July to 6 August 1985. The HRTS instrument is well suited to study the fine structure and dynamics of the solar chromosphere and transition zone by means of ultraviolet (UV) spectroscopy. We report results from analyses of some of the significant data sets from among the large number of UV spectra and spectroheliograms that were obtained during the Spacelab-2 mission.

The HRTS is a 30-cm Gregorian telescope that produces an image of the sun on

the spectrograph slit jaws with arc-second resolution. The focal-plane instrumentation consists of a tandem-Wadsworth UV spectrograph, a broadband UV spectroheliograph, and an  $H\alpha$  system. The spectrograph produces stigmatic photographic spectra of the slit, which has an equivalent length of 1

solar radius, a width of 0.5 arc sec and a corresponding spectral resolution of 50 mÅ throughout the 1200- to 1700-Å wavelength range. The broadband UV spectroheliograph uses a double-grating zero-dispersion broadband filter to photographically record the image reflected from the slit jaws. The  $H\alpha$  video image of the slit jaws is displayed on the shuttle aft flight deck for target selection and telescope focusing and is also recorded for analysis after the flight.

A broadband UV spectroheliograph image of the solar limb observed during Spacelab-2 is shown in Fig. 1. This figure shows an image of the sun reflected from the two spectrograph slit jaws with the slit roughly tangent to the solar limb and three slit jaw fiducial wires running perpendicular to the slit. The UV reflectivity of the upper slit is about four times as high as the lower slit, and this accounts for the discontinuity in the intensity of the image at the slit. The UV spectroheliograph images a band of the solar spectrum centered at 1550 Å with about a 90-Å (full width at half-maximum) passband. In this spectral region there are strong transition zone lines of C IV at 1548 and 1550 Å. There are also numerous chromospheric lines of ions such as C I, Si I, Si II, and Fe II, as well as the continuum formed at 4300 to 4900 K in the temperature minimum region. On the solar disk, the spectroheliograph integrates all of the line and continuum components in the passband, and the image shows typical upper chromospheric structures such as bushes of spicules at the supergranular cell boundaries. Above the limb the emission becomes dominated by the C IV transition zone lines.

The UV limb images show at least three categories of structures: (i) spicules similar in appearance and size to  $H\alpha$  spicules, (ii) larger spicular structures called macrospicules, and (iii) nested loops of transition zone plasmas, which show highly dynamic behavior. When these images are compared with near simultaneous  $H\alpha$  images, it can be determined that a large number of individual UV spicular structures are direct extensions of some of the larger and more distinct  $H\alpha$  spicules. The C IV macrospicules have

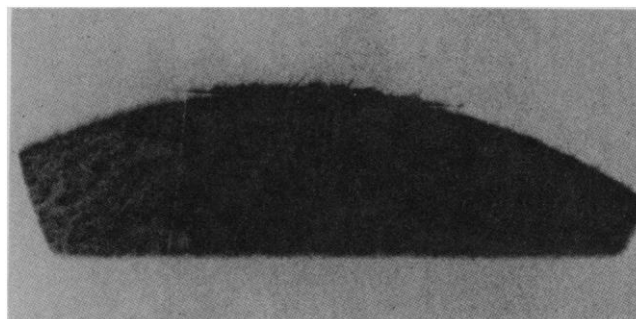


Fig. 1. Ultraviolet spectroheliograph images of C IV spicular structures at the solar limb. The distance between fiducial wires is 206 arc sec.

E. O. Hulburt Center for Space Research, Naval Research Laboratory, Washington, DC 20375.

been observed with the highest temporal resolution available. They extend to a height of 20 arc sec above the limb, as compared with 10 arc sec for the more common chromospheric spicules. During our observing period, one of these macrospicules brightened and decayed in place over the course of about 8 minutes. Some macrospicules show upward velocities on the order of 15 to 30 km/sec. When a macrospicule fades, there is evidence, at the limits of detectability, that it breaks up into small knots along its axis. The macrospicules also show motions perpendicular to their axis, as if they were following the waving of magnetic fields.

In Fig. 1, just to the left of the central fiducial wire, there is a mound-like feature that appears to be a nest of magnetic loops supporting transition zone plasma. During a 6-minute period, C IV-emitting material is seen at 15 arc sec above the nest of loops, as if it had been ejected, perhaps through the outward expansion of magnetic fields. An analysis (1) of spectra in the relatively rare regions of blueshifted emission on the disk showed that a certain subset of these regions exhibited spatial and velocity structures that could be interpreted as expulsions of plasmoids from quiet network elements in a manner similar to the phenomena observed at the limb.

At high resolution, the emission pattern on the solar disk is distributed into discrete

structures over a range of temperatures, from the temperature minimum through the transition zone. Observations of the grainy nature of the UV continuum produced in the temperature minimum have been provided (2-4). Spicules in the quiet regions and fibrils in active regions are obvious candidates for discrete chromospheric emission.

Several spectral lines and continua have been selected to display the variations in structure of the solar atmosphere over a range of temperatures. These spectra were obtained during a single sequence of exposures at a fixed pointing with exposure times ranging between 3 and 30 seconds. During this sequence, the slit was pointed so that one end intersected the solar limb and ran along a solar radius through active region McMath 4682. The spectra were digitized and processed to obtain calibrated values of solar intensity by matching average quiet region spectra to the spectrum of Kjeldseth Moe *et al.* (5). The spectra are displayed in Fig. 2. From the left are the H $\alpha$  slit jaw image in the vicinity of the slit, which runs down the center of the image; the continuum near 1615 Å; the sum of two C I intercombination lines at 1613.376 and 1613.803 Å in the 30-second exposure; the same C I intercombination lines in the 10-second exposure; the C I resonance line at 1656.266 Å in the 10-second exposure; the same C I resonance line in the 3-second

exposure; the C II line at 1335.708 Å; and the sum of the two C IV lines at 1548.202 and 1550.774 Å. For the spectra, wavelength increases to the right so that redshifted profiles are displaced to the right. The continuum at 1615 Å is formed near the temperature minimum region, and the C I lines are formed near 10<sup>4</sup> K in the chromosphere. The C II line at 1335 Å is formed at 2 × 10<sup>4</sup> K at about the same temperature as H Lyman  $\alpha$ . The spectra shown in Fig. 2 represent quiet solar regions.

The discrete emission elements along the entire slit have been identified in the spectra of the continuum near 1615 Å, the C I intercombination lines at 1613 Å, and the C IV lines. The full width at half-maximum extent of each of these structures along the slit has been measured. The discrete continuum structures and the discrete C I structures have similar size distributions and both have an average size of 2000 km. Features with sizes of 700 km (1 arc sec) have been seen in spectra recorded in this same observing period, so it is probable that the 2000-km values are not simply the product of finite telescope resolution and jitter of the Instrument Pointing System. By comparison, the size of the C IV discrete structures appears to be larger, with an average width of 2400 km. The distribution of the C IV sizes (full width at half-maximum) ranges from 1000 to 4000 km with a peak near 2000 km.

The question of the small fill factor in the transition zone has been addressed (6, 7). The present analysis calculates the fill factors from more directly measured quantities than before. We consider the intensity  $I$  of the C IV lines, which is given by

$$I = C(T) n_e^2 \Delta\ell \quad (1)$$

where  $C(T)$  is a function of temperature based on atomic data and solar elemental abundances,  $n_e$  is the electron density, and  $\Delta\ell$  is the path length. We are interested in determining sizes of the discrete structures by solving Eq. 1 for the path length  $\Delta\ell$  in terms of  $I$ ,  $n_e$ , and  $C(T)$ . The function  $C(T)$  is evaluated at 10<sup>5</sup> K, appropriate to C IV, by means of generally accepted abundances and atomic data. The electron densities are derived from measurements of the density-sensitive intensity ratios of the O IV intercombination lines near 1400 Å. The intensities of the O IV lines have been measured in the 30-second exposure at the positions of the discrete C IV elements in the slightly later 3-second exposure. For discrete structures where the O IV line intensities are too low to measure, we have assumed a uniform electron pressure of 10<sup>15</sup> cm<sup>-3</sup> K, appropriate for the quiet sun. With these densities, the path length  $\Delta\ell$  has been calculated ac-

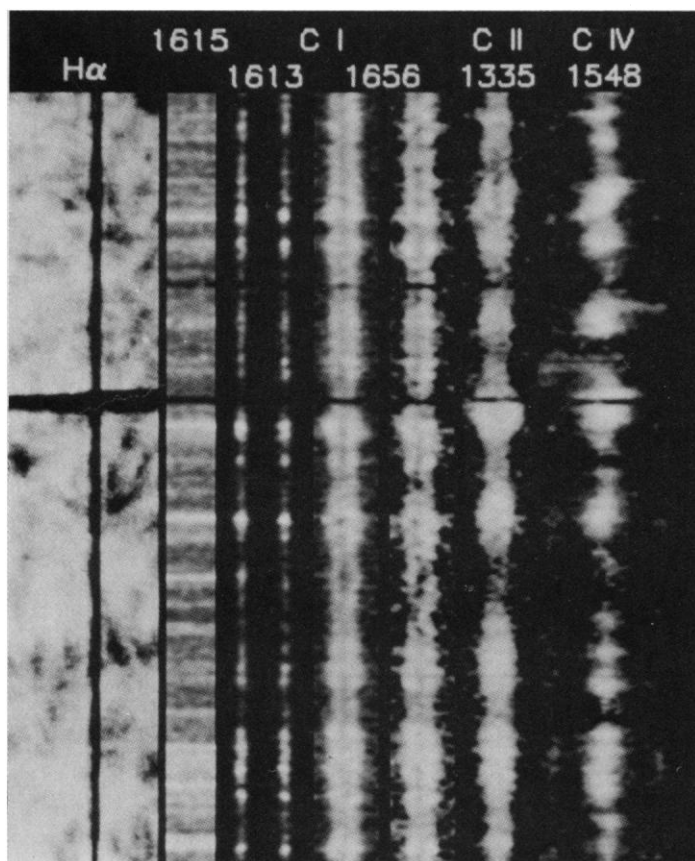


**Fig. 2.** H $\alpha$  slit jaw images and selected UV spectra over a 200-arc sec length of the slit in quiet solar regions, where  $\mu$  varies between 0.29 (at the top) and 0.67 ( $\mu = \cos\theta$ , where  $\theta$  is the angle between the normal on the sun to the line of sight).

cording to Eq. 1, which gives the path length of a layer of  $10^5$  K plasma with thickness  $\Delta\ell$  that produces the observed line intensity. The path-length distribution ranges from 0.1 to 10 km. These lengths are much smaller than the observed 2400-km extent of the structures along the slit.

The spicules and fibrils at transition zone temperatures are composed of structures that are well below the instrumental resolution. It is worthwhile to construct simple geometrical models that incorporate subresolution structures so that we may interpret the observed intensities and dimensions. Two models seem most readily applicable. In one, the transition zone consists of a thin layer that is wrapped around the chromospheric spicule. In the other, the transition zone is composed of a number of subresolution filamentary structures that are distributed throughout the spicular volume. The thickness of the transition zone in the first ("onionskin") model would be roughly half the value of the path length  $\Delta\ell$  derived above. However, the  $10^5$  K transition zone emission is not observed in a thin skin wrapped around  $10^4$  chromospheric spicules but rather in higher altitude extensions of the spicules (7). The filamentary model constructs the spicular transition zone from a loose assembly of fine filaments. If we assume each filament has the same density and cross-sectional area, then we find that the radius of each individual filament ranges between 3 and 30 km for spicules consisting of ten filaments. The derived radii scale inversely with the square root of the number of filaments assumed to fill the spicular volume. A single filament cannot explain the observed width of spicules, so it is possible to set 70 km (0.1 arc sec), the width derived assuming there is a single filament, as an upper limit to the size of these subresolution filaments. It is not possible to determine a lower limit to their sizes.

The small area fill factor of the transition zone has immediate consequences for derived fluxes of material and energy through the transition zone. For example, it is estimated that coronal energy losses in the quiet sun are dominated by the conductive losses through the transition zone (8). This conclusion is based on the assumption of a plane-parallel solar atmosphere. When the areal fill factor of spicular structures ( $10^{-5}$  to  $10^{-2}$ , calculated for the filamentary models but approximately the same for the onionskin model) is taken into account, the derived conductive losses will be reduced by this same factor. Furthermore, the observed temperature gradients along magnetic field lines in the quiet sun are on the order of two magnitudes lower than those derived under the plane-parallel assumption. Thus, the

conductive flux from the corona through observed transition zone structures is negligible compared to coronal radiative losses.

The microscopic transition zone structures must be intimately related to the local heating mechanism, which might operate on microscopic scales but would also explain fundamental macroscopic characteristics of the transition zone. The heating is local because the shallow temperature gradients in the transition zone do not support a significant conduction of energy from the corona. Recently, it has been shown that coronal loops can be heated by the resonant absorption of Alfvén waves and that this dissipation occurs on spatial scales of 0.3 to 250 km, transverse to the magnetic field direction (9, 10).

#### REFERENCES AND NOTES

1. K. P. Dere, J.-D. F. Bartoe, G. E. Brueckner, *Astrophys. J.* **310**, 456 (1986).
2. G. E. Brueckner, in *Highlights of Astronomy*, P. A. Wayman, Ed. (International Astronomical Union, Reidel, Dordrecht, Netherlands, 1980), vol. 5, pp. 557-569.
3. R. M. Bonnet *et al.*, *Astron. Astrophys.* **111**, 125 (1982).
4. J. W. Cook, G. E. Brueckner, J.-D. F. Bartoe, *Astrophys. J.* **270**, L89 (1983).
5. O. Kjeldseth Moe, M. E. VanHoosier, J.-D. F. Bartoe, G. E. Brueckner, *Naval Research Laboratory Report 8057* (1976).
6. U. Feldman, G. A. Doschek, J. T. Mariska, *Astrophys. J.* **229**, 369 (1979).
7. K. P. Dere, J.-D. F. Bartoe, G. E. Brueckner, *ibid.* **305**, 947 (1986).
8. G. L. Withbroe and R. W. Noyes, *Annu. Rev. Astron. Astrophys.* **15**, 363 (1977).
9. J. M. Davila, *Astrophys. J.* **317**, 514 (1987).
10. G. Einaudi and Y. Mok, *ibid.* **319**, 520 (1987).

26 May 1987; accepted 31 August 1987

## A Cell-Cycle Constraint on the Regulation of Gene Expression by Platelet-Derived Growth Factor

BARRETT J. ROLLINS, ELIZABETH D. MORRISON, CHARLES D. STILES

**In density-arrested monolayer cultures of Balb/c 3T3 cells, platelet-derived growth factor (PDGF) stimulates expression of the *c-myc* and *c-fos* proto-oncogenes, as well as the functionally uncharacterized genes, JE, KC, and JB. These genes are not coordinately regulated. Under ordinary conditions, *c-fos*, JE, KC, and JB respond to PDGF only when the cells are in a state of  $G_0$  growth arrest at the time of PDGF addition. The *c-myc* gene is regulated in opposition to the other genes, responding best to PDGF in cycling cultures.**

**P**LATELET-DERIVED GROWTH FACTOR (PDGF) exerts its mitogenic effect on mouse fibroblasts, in part, by inducing the expression of otherwise silent genes (1-3). The proto-oncogenes *c-myc* and *c-fos* are among these genes, and appear to function as intracellular mediators of the growth response to PDGF (4, 5). PDGF also induces the expression of several other genes, designated JE, KC, and JB, which are functionally uncharacterized (1). As a first step toward understanding the function of these genes, we have undertaken experiments to analyze the controls governing their PDGF-induced expression. If genes like JE, KC, and JB have functions analogous to those of *c-myc* and *c-fos*, we would expect that their expression might be regulated in similar ways.

Contrary to expectations, noncoordinate control of PDGF-inducible gene expression

was displayed during the course of a cell growth experiment (Fig. 1). Balb/c 3T3 cells were plated at very low density and then grown to confluence in serum-supplemented medium (6). Steady-state levels of *c-myc* messenger RNA (mRNA) were highest when cells were sparse and decreased steadily as the cells approached confluence and growth arrest. In contrast, JE mRNA was undetectable in sparse cultures and rose to high levels only as the cultures approached the confluent monolayer state. The *c-myc* gene still showed some expression at high cell density because of continuous exposure to serum.

Serum contains several factors that regulate 3T3 cell growth. To determine whether this cell-density effect on gene expression reflected a differential response of the *c-myc* and JE genes to PDGF, we plated Balb/c 3T3 cells sparsely (about 1/40 of confluent density) and incubated them in PDGF-free medium supplemented with 5% platelet-poor plasma (PPP) (7). The steady-state level of *c-myc* mRNA in these sparse, PDGF-starved cell cultures was low (Fig. 2A). Treatment with PDGF led to a sizable

B. J. Rollins, Division of Medicine, Dana-Farber Cancer Institute and Harvard Medical School, Boston, MA 02115.

C. D. Stiles and E. D. Morrison, Department of Microbiology and Molecular Genetics, Harvard Medical School and Dana-Farber Cancer Institute, Boston, MA 02115.